Available online at www.sciencedirect.com

jmr&t Journal of Materials Research and Technology

journal homepage: www.elsevier.com/locate/jmrt

Original Article

Effect of temperature on shielding efficiency of phosphate-bonded $CoFe_2O_4 - xBaTiO_3$ multiferroic composite ceramics in microwaves

D. Meisak [a,*], A. Plyushch [a], J. Macutkevič [a], R. Grigalaitis [a], A. Sokal [b], K.N. Lapko [b], A. Selskis [c], P.P. Kuzhir [d], J. Banys [a]

[a] Faculty of Physics, Vilnius University, Sauletekio Al. 9, Vilnius, LT-10222, Lithuania
[b] Affiliation-independent researchers
[c] Center for Physical Sciences and Technology, Sauletekio Al. 3, Vilnius, LT-10257, Lithuania
[d] Department of Physics and Mathematics, Institute of Photonics, University of Eastern Finland, Yliopistokatu 7, Joensuu, FI-80101, Finland

ARTICLE INFO

Article history:
Received 13 January 2023
Accepted 17 March 2023
Available online 22 March 2023

Keywords:
Phosphate-bonded ceramics
Barium titanate
Cobalt ferrite
EMI shielding efficiency
Microwaves

ABSTRACT

A series of novel $CoFe_2O_4 - xBaTiO_3$ ($x = 0.6–0.9$) phosphate-bonded multifunctional ceramic composites were synthesized and studied both in 'Salisbury screen' geometry and as free-standing films in the frequency range of 25–54 GHz and temperature interval of 120–500 K. Experiments prove that the studied system is prospective for shielding applications in both modes providing total transmission losses of the free-standing sample layer of 40 dB for $x = 0.9$ dominated by absorption and more than 40 dB of reflection losses at resonant conditions in the Salisbury screen geometry. It was demonstrated that the electromagnetic response of multiferroic composite ceramics in microwaves is very sensitive to the temperature changes in the application's significant temperature range, i.e. 150 – 400 K. Notably, a small, i.e. 5 – 10 K, temperature variation drastically changes the shielding efficiency of the Salisbury screen (SE_R). In particular, $SE_R \geq 40$ dB is achieved in the range of 302–309 K for the sample with $x = 0.9$, outside of the range SE rapidly decreases to 10–15 dB. The impact of temperature has to be considered for the efficient use of shielding materials in Ka and V bands for different applications.

1. Introduction

Electromagnetic (EM) shielding usually refers to attenuation of the radio-frequency or microwave radiation. Two different cases are distinguished for a planar geometry, i.e. non-reflective shielding surfaces with back reflectors (known as Salisbury screen) and free-standing non-transmitting layers of the radar absorbing material. Salisbury screens are widely used in radio-to THz frequency ranges. Their potential applications include but are not limited to

* Corresponding author.
E-mail address: darya.meisak@ff.vu.lt (D. Meisak).
https://doi.org/10.1016/j.jmrt.2023.03.124

antennas, radars, anechoic chambers, cloaking, imaging, and sensing applications [1–4]. Free-standing films are operated in a different mode. The purpose of such films is to provide as low transmission as possible in combination with high absorption. That is extremely important now in the 5G era due to EM interference (EMI) problems. EMI issues may not only seriously affect the regular operation of electronics but also causes potential risks to human health [5–7]. Most EMI tasks require shielding materials to be effective at a particular temperature, corresponding to the operational conditions, e.g. in the case of CPUs or GPUs, it is 80–90 °C; for avionics and cryogenics, the range is much lower, down to a couple of K. A material which shields perfectly at room temperature might fail at other ones.

In recent decades, a variety of very different materials and structures were examined for EMI applications. Among them are composites with the addition of carbon nanotubes [8–11], graphene nano platelets [12,13], and graphene oxide [14], also metasurfaces [15–17], and ceramics [18–22]. Despite the significant progress, just a few works [12,23,24] have been focused on the temperature impact on the shielding efficiency (SE). In contrast, tiny temperature variations might dramatically influence the electromagnetic response of the composite, suppressing EMI SE. Depending on the particular applications, temperature could be changed due to external conditions or heat due to absorbed EM energy.

Previously it was demonstrated that the phosphate-bonded ceramics (PBC) are prospective candidates for EM shielding applications [18,25]. The PBC approach benefits an easy and eco-friendly preparation procedure. Namely, powders are bonded with liquid or solid phosphate glue but not sintered. The main properties of cured bonded ceramics, such as thermal and mechanical stability, corrosion, and wear resistance, are comparable to the ones of the conventionally sintered counterparts [26]. Such approach allows to avoid the unexpected reactions between components upon sintering. This is important for ceramics with carbonaceous inclusions [27] or multiferroics [28]. The wide list of applications of PBCs includes medicine [29,30], electronics [31–33], production of the anti-corrosion coatings [34,35], radiation and EM shielding applications [18,36,37].

Compositions with the addition of the magnetic inclusions [9,38], hexaferrites [39,40] or spinels ($CoFe_2O_4$, or $NiFe_2O_4$) [41–44] provide the level of SE of >20 dB due to high reflection losses caused by the Ohmic losses of magnetic particles. Ferroelectrics, like $BaTiO_3$, provide high dielectric permittivity and thus are prospective for EM shielding applications in microwaves [45–47]. One can expect enhanced SE by combining two types of components due to the superposition of different shielding mechanisms [48]. The present work is devoted to the preparation of $CoFe_2O_4 - xBaTiO_3$ (x = 0.6–0.9) phosphate-bonded ceramics. The phosphate bonding is a novel approach for synthesizing composite magnetoelectric ceramics avoiding sintering. The dielectric properties and shielding efficiency were explored in Ka and V bands in two different modes, $\lambda/4$ geometry with a back reflector (Salisbury screen) and as a free-standing layer. The impact of temperature on the SE was studied for both modes within the 120–500 K range.

2. Materials and methods

For the experimental exploration of the influence of temperature on SE, a series of multiferroic $CoFe_2O_4 - xBaTiO_3$ (x = 0.6–0.9, mass ratio) phosphate-bonded composite materials were prepared and studied in 25–54 GHz frequency range and 120–500 K temperature interval. The samples were prepared as follows. $BaTiO_3$ (208,108, grain size < 3 μm) and $CoFe_2O_4$ (773,352, mean grain size of 30 nm) powders were purchased from Sigma-Aldrich. The aluminium phosphate binder (APB) was obtained by the acid-base interaction of an aqueous suspension of aluminium hydroxide $Al(OH)_3$ in concentrated orthophosphoric acid H_3PO_4 (85 wt %) and then the mixture was heated up to 373 K during continues stirring before the complete dissolution of hydroxide took place. The mole ratio of H_3PO_4 and $Al(OH)_3$ was equal to 3:1. Being prepared, the obtained transparent viscous solution of APB was diluted with distilled water to a density of 1.42 g/cm^3. The powders were mixed in appropriate proportions with a total weight of 1 g in an agate mortar, and then 0.05 g of binder was added. The obtained mixture was homogenized and pressed uniaxially into tablets of a diameter of 1 cm under 6 tons. After 24 h at room temperature, the samples were heated to 600 K to speed up curing. More details on the preparation procedure and properties, i.e. thermal stability, magnetic properties, and magnetoelectric coupling, are presented in the previous work [49]. Further samples are labelled as CFO-xBTO.

The refraction index $n = \sqrt{\varepsilon\mu}$ in 25–54 GHz was measured with the two waveguide systems: 25–40 and 40–54 GHz. A thin rod of the sample was placed perpendicularly to the broader wall of the waveguide, and the scattering parameters S_{11} and S_{21} were measured using scalar network analyzers Elmika (Vilnius, Lithuania). The refraction index was recalculated as described in paper [50]. Using measured material parameters, the SE of the thin layer of the sample was recalculated. Measurements above or below room temperature were carried out using a custom-made cryostat system with liquid nitrogen for cooling and a custom-made furnace for heating. Scanning electron microscopy (SEM) with energy dispersive X-ray analysis (EDX) was performed on Helios NanoLab 650 microscope. The X-ray diffraction (XRD) analysis was carried out on a DRON 3.0 diffractometer using CoK α radiation ($\lambda = 1.78896$ Å), the COD database [51] was applied for the identification.

3. Results and discussion

The X-ray diffraction patterns of the CFO-xBTO samples are presented in Fig. 1. The peaks are identified as the tetragonal P4mm $BaTiO_3$ (1,507,756) and cubic Fd3m $CoFe_2O_4$ (1,535,820) phases. Reflections from the (002) and (200) planes of $BaTiO_3$ are split, proving the tetragonal distortion of the crystal lattice typical to the ferroelectric state. As the loading of $BaTiO_3$ increases, the intensity of the peaks from $CoFe_2O_4$ gradually decreases, and finally, for CFO-0.9BTO, only one (311) peak remains at 41.6°. The absence of unexpected peaks proves the purity of the CFO and BTO phases.

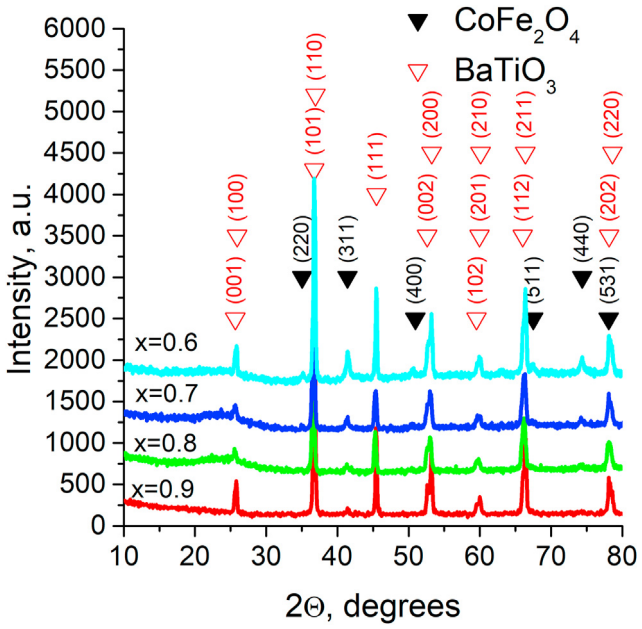

Fig. 1 – X-ray diffraction patterns of the studied CFO-xBTO samples with different x content.

Scanning electron microscopy images of CFO-0.7BTO with EDX mapping are presented in Fig. 2. Brighter points in EDX correspond to the presence of the selected element. Their relative amounts are collected in EDX Table 1t in Supplementary materials. Phosphorus only appears in phosphate binder, so it is situated between grains of $BaTiO_3$ or $CoFe_2O_4$. Therefore, the uniform distribution of phosphorus indicates the homogeneity of the composite. In the studied case, only several areas where the amount of phosphorus is higher were found. The distribution of cobalt is similar to the one of phosphorus, but the only difference is the presence of darker regions. One brighter zone on the Co map corresponds to a darker one on the Ba map. That is likely an agglomerated $CoFe_2O_4$. The map of $BaTiO_3$ slightly differs from others due to a noticeable amount of brighter zones. In this case, zones correspond to grains of $BaTiO_3$, rather than agglomerates.

The temperature dependence of the real and imaginary parts of the refraction index is presented in Fig. 3(a). An increase in the content of $BaTiO_3$ gains both n' and n''. At the same time, the samples with an amount of $BaTiO_3$ higher than 0.6 demonstrate a series of anomalies near 200, 300, and 410 K. These anomalies are attributed to the phase transitions from cubic phase to tetragonal close to 410 K, next to orthorhombic at 300 K, and finally to rhombohedric at 200 K [55]. As x decreases, the peaks vanish, and eventually, n of $CoFe_2O_4$ - $0.6BaTiO_3$ only weakly depends on temperature. Frequency spectra of n' and n'' of the samples reveal no significant dispersion within the studied range (see Fig. 3(b) and Fig. 1(s) in Supplementary Materials.

3.1. *Shielding efficiency in salisbury screen geometry*

Salisbury screen comprises a layer of material placed on a back-reflector. Its effectiveness is determined by the resonant $\lambda/4$ condition [45]:

$$d_m = \frac{m}{4}\frac{c}{\nu_m n}, \quad (1)$$

where d_m is a thickness of a layer, c is the speed of light in vacuum, ν_m is the frequency of the incident radiation, n is a refraction index and m = 1,2,3 … is natural number. Upon this,

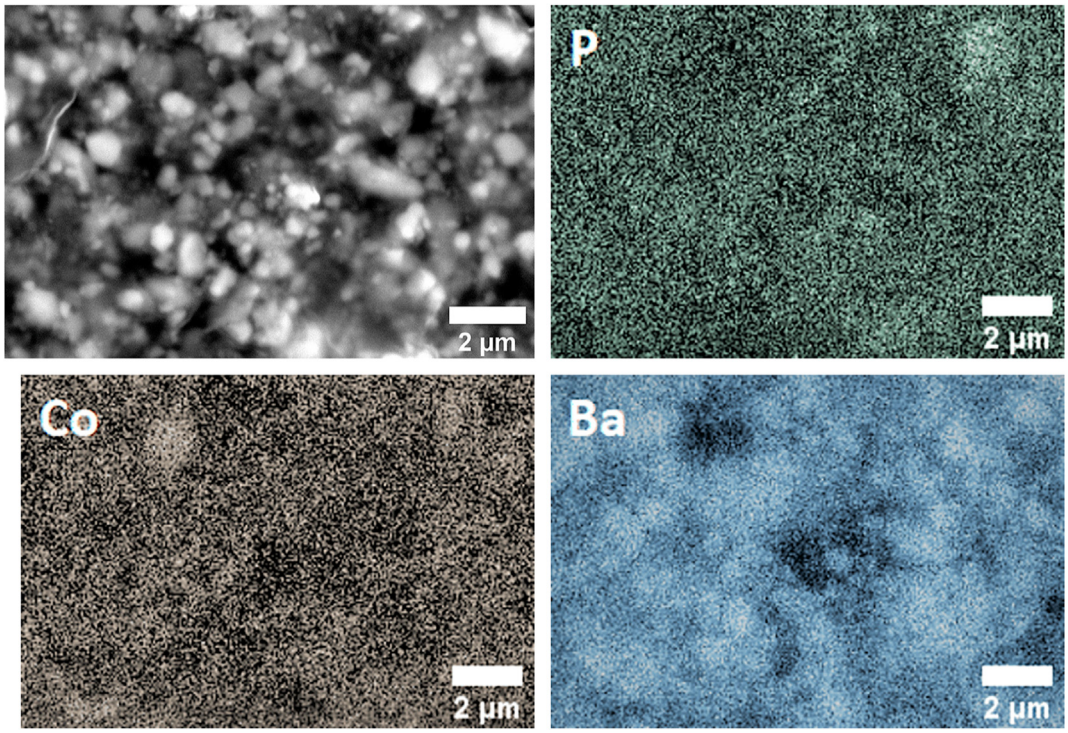

Fig. 2 – Scanning electron microscopy images and elemental distributions maps of the sample CFO-0.7BTO.

Table 1 – Comparison of the SE_T of various materials.

Material	Thickness, mm	Frequency, GHz	SE_T, dB	Reference
$ZnNb_2O_6$-chopped strands/epoxy	1.5	17.52	31.1	[52]
Carbon nanotube (CNT)/$BaFe_{12-x}Ga_xO_{19}$/epoxy	2.6	45	13	[40]
$CoFe_2O_4$/polyaniline	4	8–12	22.5	[41]
CF-PTh/graphene	n/a	18	26	[53]
Graphene/natural rubber	3	18	5–20	[54]
CNT/barium titanate	2.5	30	27	[46]
CNT/TiO_2/epoxy	2	35	20	[9]
CNT/Fe/epoxy	2	35	32	[9]
ZrB_2 nanoparticles/PDC-SiOC ceramic	3	39.7	90.8	[19]
Phosphate-bonded CFO-0.9BTO	4	45	40	present research

two reflected waves interfere, which suppress the total reflection down to zero. Eq. (1) gives the optimal thickness d_m for any ν_m and n of a lossless material. Dielectric or magnetic losses substantially change the situation due to the rotation of the phase angle. As a result, only a certain set of combinations of the thickness of the layer and its' refraction index n at the selected frequency satisfy the resonance [25]. Both material parameters, the dielectric permittivity ε and magnetic permeability μ, are temperature-dependent, which brings additional complexity to the system. Knowing how the system will act under different temperatures is important for optimizing the material for a certain application.

The shielding efficiency of Salisbury screens is determined as $SE_R = |20log_{10}(S_{11})|$. The scattering parameter $S_{11}(\lambda, d, \varepsilon, \mu)$ is a ratio of the amplitudes of the incident and reflected signals $S_{11} = E_{ref}/E_{in}$:

$$S_{11} = -\frac{k_z(exp\{2idk_{2z}\} - 1) + k_{2z}(1 + exp\{2idk_{2z}\})}{k_z(1 - exp\{2idk_{2z}\}) + k_{2z}(1 + exp\{2idk_{2z}\})}, \quad (2)$$

where $k_z = 2\pi/\lambda$ and $k_{2z} = 2\pi\sqrt{\varepsilon\mu}/\lambda$ are the wave numbers in a vacuum and the material correspondingly, d is the thickness of the composite, and λ is the wavelength. A non-magnetic material with $\mu = 1$ is considered for the modelling. Such a simplification is relevant for a wide range of non-magnetic materials with carbonaceous inclusions [8–10,12–14], semiconductors [18], or ferroelectrics [45–47,56]. In general case ε depends on temperature and frequency, *i.e.* $\varepsilon = \varepsilon(T, \omega)$. One of the most common forms of the $\varepsilon(T)$ dependence is relaxation. Then, the dielectric permittivity follows the Debye equation or similar, like Cole-Cole formula [57,58]:

$$\varepsilon = \varepsilon_\infty + \frac{\varepsilon_s - \varepsilon_\infty}{1 + (i\omega\tau)^{1-\alpha}}. \quad (3)$$

where α changes in a range of 0–1 and demonstrates flattening of the maximum of the imaginary part of dielectric permittivity, $\varepsilon_0 = \lim_{\omega\to 0}\varepsilon(\omega)$, $\varepsilon_\infty = \lim_{\omega\to\infty}\varepsilon(\omega)$. All parameters in Eq. (3) depend on the temperature in the general case. Usually, the dependence of the relaxation time follow Arrhenius law, $\tau(T) = \tau_0\, Exp(E_a/kT)$, or Vogel-Fulcher law. Arrhenius law behaviour is typical for the majority of materials from ferroelectrics [59,60] to polymer-based composites [61,62], while Vogel-Fulcher law describes glass transitions in polymers [63,64], or dynamics in relaxor ferroelectrics [65]. Here E_a is the activation energy. Next, ε_∞, ε_s, and α are considered temperature-independent and equal to 30, 430, and 0.5, respectively. This simplification is possible since within a narrow temperature range of 10–20 K, the dynamics of ε are mostly determined by the shift in

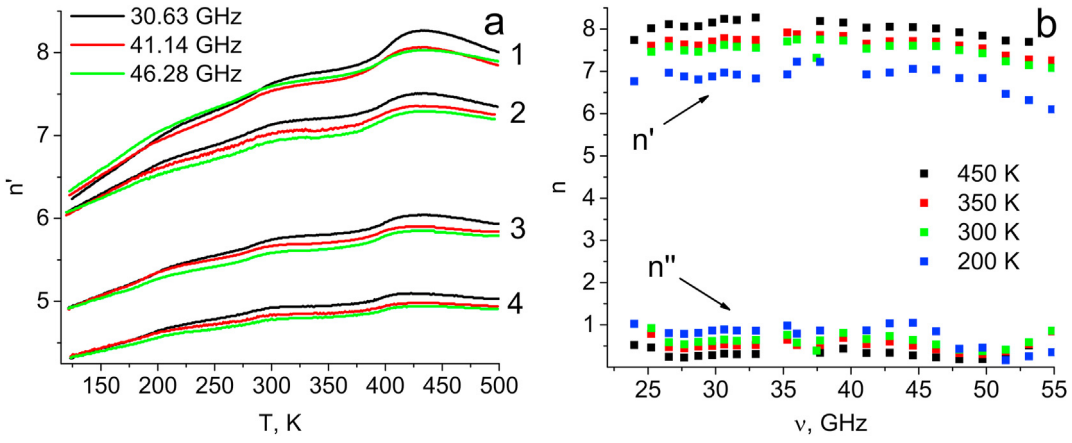

Fig. 3 – Refraction index of the phosphate-bonded $CoFe_2O_4$ - $xBaTiO_3$ as a function of temperature: 1 - CFO-0.9BTO, 2 - CFO-0.8BTO, 3 - CFO-0.7BTO, and 4 - CFO-0.6BTO (a). Frequency dependence of the refraction index of CFO-0.9BTO at different temperatures (b).

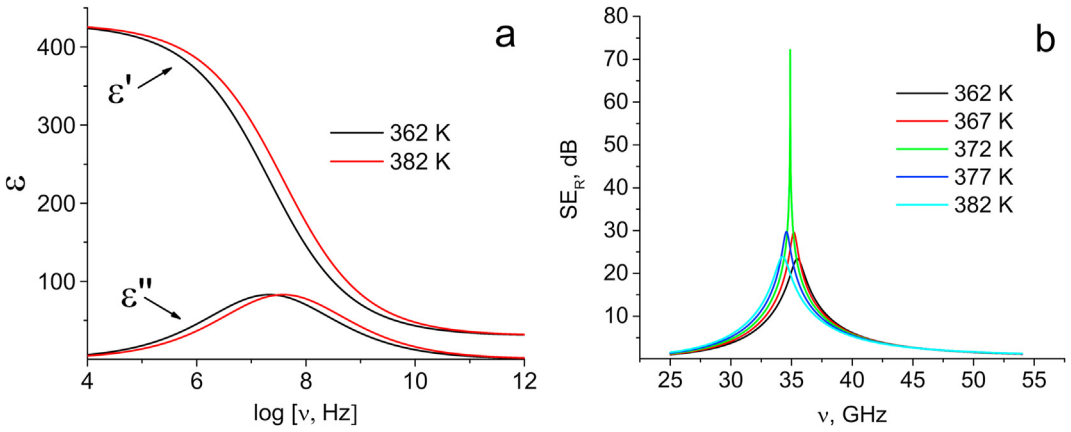

Fig. 4 – Real and imaginary parts of the dielectric permittivity calculated with Eq. (3) at different temperatures (a). SE_R at different temperatures as a function of frequency (b).

relaxation, neither flattering nor variations in ε_s. The variation of the relaxation time τ is described by Arrhenius law with the following parameters: $\tau_0 = 10^{-13}$ s and $E_a = 0.35$ eV. Such a value of the E_a is slightly higher than one typical for ferroelectrics [59,60], but it fits carbonaceous-based binary [66] and ternary [62] composites.

The dielectric permittivity calculated at temperatures of 362 and 382 K is presented in Fig. 4(a). The maximum of ε'' is below 10^8 Hz, which is two orders of magnitude lower than the studied range of 25–55 GHz. Both real and imaginary parts of permittivity undergo tiny variations when the temperature changes from 362 to 382 K.

For the calculation of SE_R, the thickness of the sample layer was taken as 0.35 mm following the $\lambda/4$ condition. The results are presented in Fig. 4(b). The shielding efficiency of the material layer with the back reflector drastically changes in the studied interval of temperatures. In particular, SE_R at 372 K demonstrate a sharp peak approaching 70 dB at 34.86 GHz. At temperatures of 367 K and 377 K, it decreases twice and maximum shifts symmetrically to higher and lower frequencies correspondingly. Further changes in temperature suppress the maximum even more. For several applications, SE_R of 20 dB is still acceptable, but additional heating or cooling leads to a further decrease in shielding efficiency.

The simple numerical model proves that tiny (5–10 K) variations in temperature impact SE_R noticeably. However, the dielectric permittivity of the actual samples is not always described only with the relaxation function since different processes of other nature may occur. Phase transitions bring anomalies in real and imaginary parts of ε, conductivity at low frequencies impacts the dielectric losses in microwaves, and even materials with more than one relaxation are not rare [67,68].

Combining Eq. (2) and data in Fig. 3 the SE simplifies to the function of 3 variables: SE=SE $(n'(T), n''(T), d, \omega)$. The particular case of the SE_R for CFO-0.8BTO at a resonant thickness of 0.274 mm is presented in Fig. 5. SE depends on the temperature similar to the numerically predicted results (Fig. 4,b): with the increase in T, the peak decreases and shifts to lower frequencies.

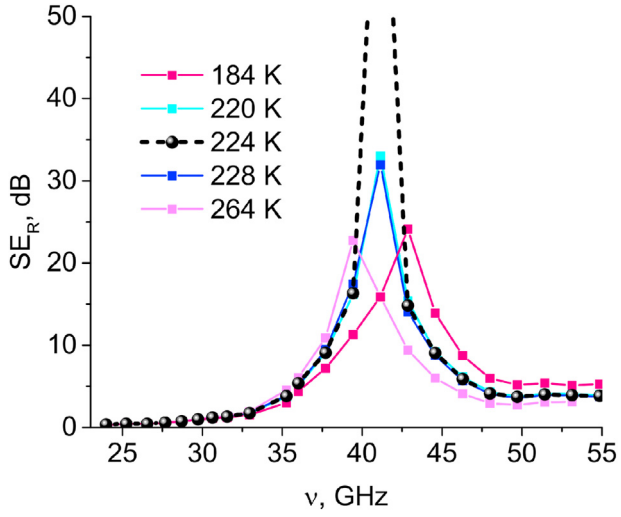

Fig. 5 – SE_R at different temperatures as a function of frequency for CFO-0.8BTO at 0.274 mm of thickness.

To study the system in general, the following technique may be proposed. First, the working frequency was considered fixed. This additionally simplifies the SE_R function. The combinations of d and $n(T)$, that fulfil the condition of SE_R $(n(T), d)$ > SE_{R0} represent a set of points on the d(T) plane. The results are collected in Fig. 6.

Each composition in Fig. 6 has a narrow range in temperature and thickness where it is optimal for EM shielding applications as Salisbury screen at considered frequency. In particular, CFO-0.8BTO with a thickness of 0.36 mm at 30.6 GHz provides SE_R > 40 dB in a temperature range of 223–238 K. Outside this range, the shielding efficiency continuously decreases to 10 dB. At higher frequencies, the optimal interval shifts to lower T and d, and narrows. The variations in the loading with $BaTiO_3$, x also impact the shielding efficiency. Within the increase in x, the required thickness of the layer decreases, and the working temperature range shifts closer to room temperatures. The reduction in $BaTiO_3$ content causes the lack of shielding performance. SE_R

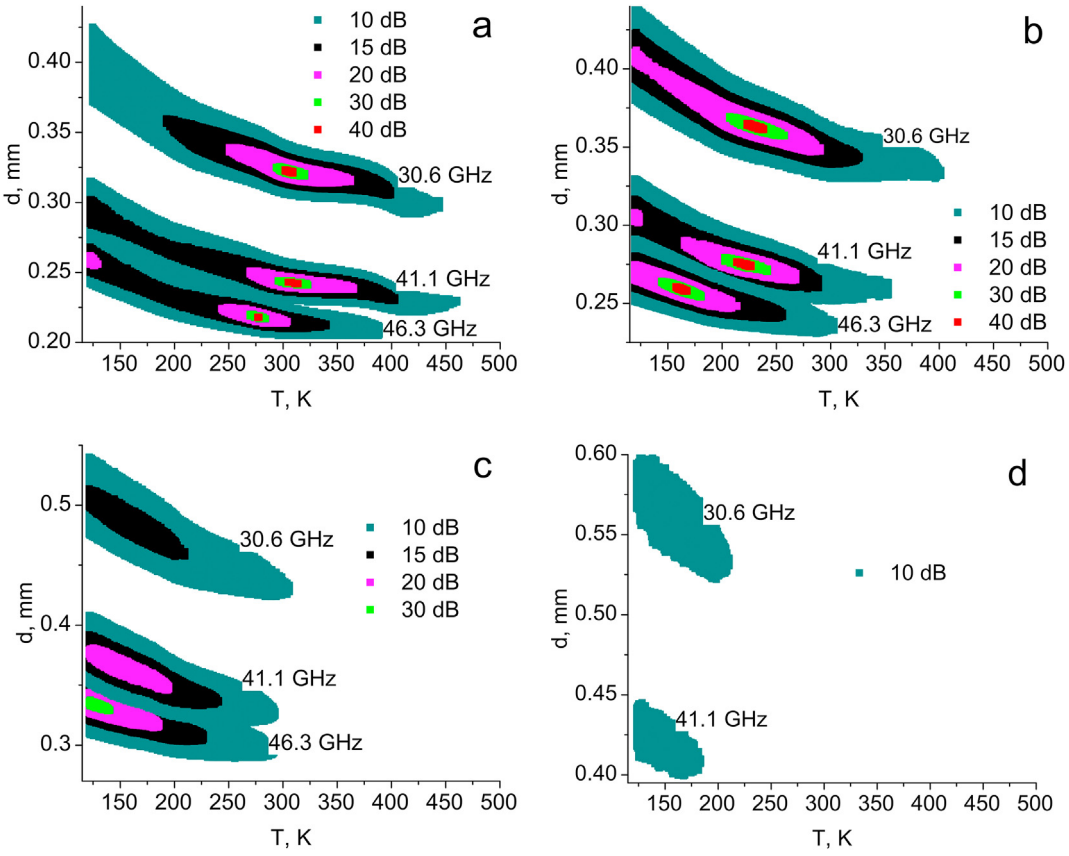

Fig. 6 – SE_R at different thickness of the layer d and temperature of CFO-0.9BTO (a), CFO-0.8BTO (b), CFO-0.7BTO (c), and CFO-0.6BTO (d).

of samples with x = 0.9 and 0.8 is more than 40 dB for all selected frequencies sample with x = 0.7 reaches 30 dB only at 46.3 GHz. And finally, there is no combination of T and d for CFO-0.6BTO to shield more than 15 dB.

The substantial difference between studied materials is the content of BTO and CFO. A CFO substitution with BTO changes the total dielectric permittivity, permeability, and temperature dependencies. As a result, it makes the refraction index of the composite match the resonant condition for the studied frequency range at particular temperatures. A similar effect was achieved for single-phase and composite multiferroics: La-doped $BiFeO_3$ [23,24], carbon nanotubes – $BaTiO_3$–Fe_3O_4 [25].

3.2. *Shielding ability of the free-standing layer*

The transmission of the free-standing film layer at different temperatures was estimated using the approach described in Refs. [69,70]. S-parameters (S_{11} and S_{21}) were evaluated for the 4 mm film layer in free space. Reflection, transmission and absorption are reads: $R = |S_{11}|^2$, $T = |S_{21}|^2$, and A = 1-R-T, respectively. The absorption coefficient, defined as the ratio of the absorbed to the incident power of the EM wave, does not represent the ability of the layer to absorb since some part of the wave is already reflected at the interface and does not enter the layer. Due to this, the effective absorption coefficient, A_{eff}, can be defined as A_{eff}=(1-R-T)/(1-R) [12]. Knowing R, T, and A_{eff}, the shielding efficiency of the material evaluated as follows [71]:

$$SE_R = -10log_{10}(1-R), \quad (4)$$

$$SE_A = -10log_{10}(1-A_{eff}), \quad (5)$$

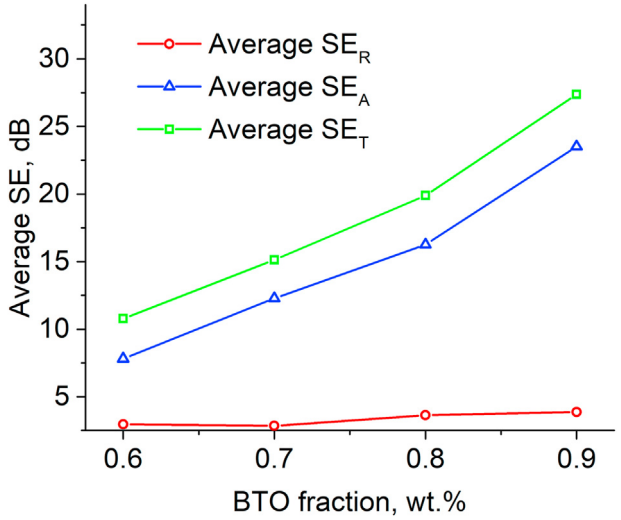

Fig. 7 – Average reflection and absorption losses and total shielding efficiency over the Ka and V bands at room temperature.

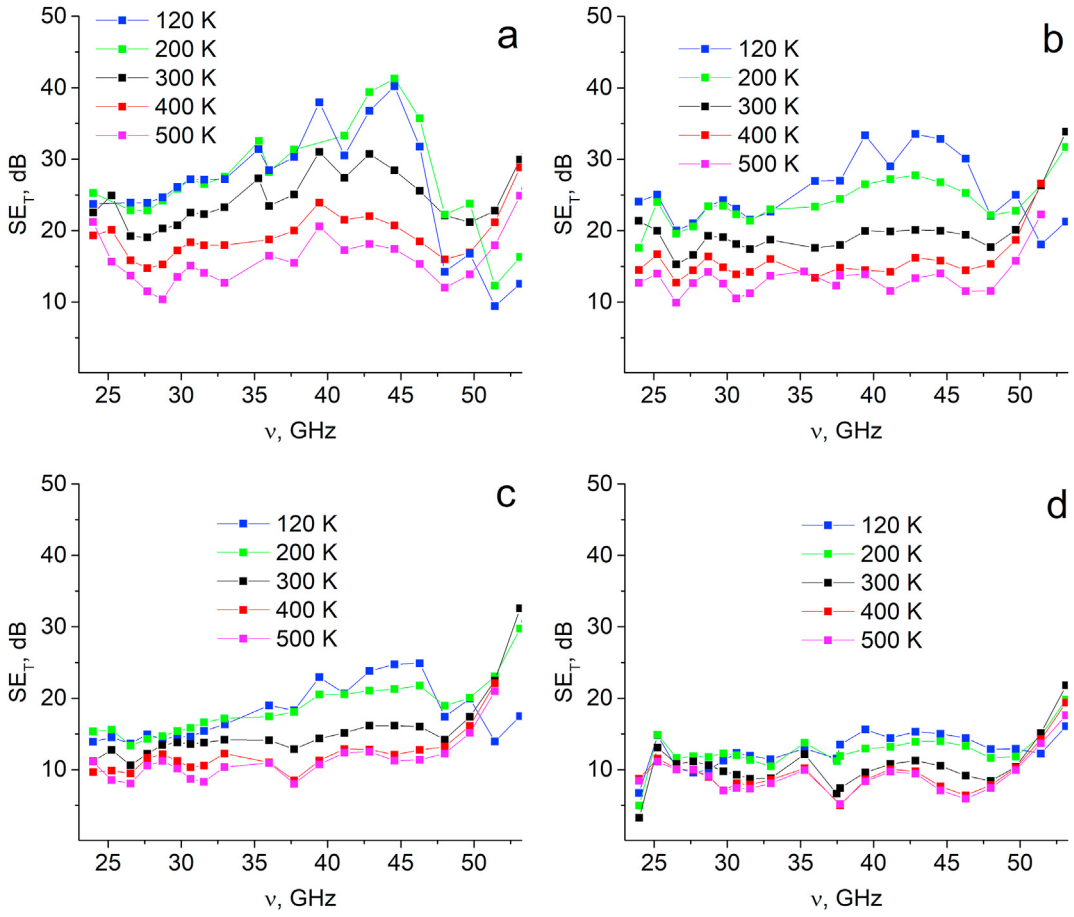

Fig. 8 – SE$_T$ of the 4 mm layer of CFO-0.9BTO (a), CFO-0.8BTO (b), CFO-0.7BTO (c), and CFO-0.6BTO (d).

$$SE_T = SE_A + SE_R. \quad (6)$$

The dependence of the average shielding efficiency over the studied frequency range on the content of $BaTiO_3$ at 300 K is presented in Fig. 7. The dominant mechanism of shielding for all examined samples is absorption. With the increase in x to 0.9, the absorption losses increase more than twice. The reflection losses only weakly change with the variations of the composition. The total shielding efficiency reaches 30 dB for the CFO-0.9BTO sample layer. Therefore the composite system is promising for many applications and comparable to novel shielding materials (see Table 1).

The frequency dependencies of SE$_T$ of composites at different temperatures are collected in Fig. 8. The partial impacts of SE$_A$ and SE$_R$ on the total shielding are presented in Supplementary materials, Figs. 2s and 3s. A maximum of SE$_T$ ≈ 40 dB is found at a frequency of 45 GHz and a temperature of 120 K for CFO-0.9BTO. As the temperature increases, the maximum broadens and shifts to lower frequencies. All composites demonstrate a similar trend: with an increase in temperature, both SE$_A$ and SE$_R$ decrease. The resulting downturn in SE$_T$ originated from the drawback of the absorption losses rather than reflection ones. The reflection losses are directly related to the charge density at the surface of the composite. The mechanism of absorption in the studied system is unclear. The loss tangent is low (see Fig. 4), so the electric conductivity is not a favourable mechanism. The temperature behaviour of SE$_T$ of the studied system is also different compared to the one of the conductive graphene-based composites [12]. The scattering due to multiple reflections at the borders of $BaTiO_3$ grains separated with nanosized grains of $CoFe_2O_4$ of relatively lower permittivity and higher dielectric losses is the more preferable mechanism. The dynamics of dielectric permittivity of BTO and CFO are different: $\varepsilon(T)$ of CFO rapidly increases with grows of temperature, while the one of BTO demonstrates phase transition-related anomaly and decreases following Curie-Weiss law. That vanishes the difference of ε of different phases at higher temperatures. As a result, it suppresses absorption losses.

4. Conclusions

The multiferroic $CoFe_2O_4$-x$BaTiO_3$ (x = 0.6–0.9) composites materials were prepared via PBC approach and examined as EM absorber in microwaves (Ka and V bands) both in free-standing mode and Salisbury screen geometry. It was proved that the proposed material is prospective for both cases. The total transmission losses of the sample layer reach 40 dB for CFO-

0.9BTO with the domination of the absorption loss. For the Salisbury screen geometry, the reflection losses exceed 40 dB. Together with previously measured magnetoelectric coupling [49], the reported properties make the novel material multifunctional, suitable both for magnetoelectric and shielding applications. The impact of temperature on SE was studied within the range of 120–50 K. Simple numerical model demonstrates that a tiny variation in T drastically changes the shielding performance of the Salisbury screen. Experiments prove that temperature significantly impacts SE_R and SE_T. In particular, the absorption losses of the CFO-0.9BTO layer decrease from 37 to 12 dB at 45 GHz as the temperature increases from 120 to 500 K. The system with the back reflector is, as expected, more temperature-sensitive. However, even for the system out of resonance, the SE_R is higher than 40 dB within the interval in T of 15–20 K (See Fig. 6). Depending on the composition *x*, the optimal material for room temperature, higher or lower temperature applications can be selected.

Credit authorship contribution statement

D.Meisak: Investigation, Data curation, Writing Original Draft. A. Plyushch: Conceptualization of this study, Methodology, Writing, Review and Editing. J. Macutkevič: Writing, Review and Editing. R. Grigalaitis: Writing, Review and Editing, Supervision. A. Sokal: Investigation, Data curation. K.N. Lapko: Investigation, Supervision. A. Selskis: Visualization. P.P. Kuzhir: Supervision, Writing, Review and Editing. J. Banys: Supervision.

Declaration of competing interest

The authors declare that they have no known competing financial interests or personal relationships that could have appeared to influence the work reported in this paper.

Acknowledgements

AP was supported by funding from the European Social Fund (project no. 09.3.3-LMT-712-19-0146) under a grant agreement with the Research Council of Lithuania (LMTLT). PK is supported by the Academy of Finland via Flagship Programme Photonics Research and Innovation (PREIN), decision 320166, grant 343393, and TERASSE H2020 RISE Project Number: 823878.

Appendix A. Supplementary data

Supplementary data to this article can be found online at https://doi.org/10.1016/j.jmrt.2023.03.124.

REFERENCES

[1] Panwar R, Lee JR. Recent advances in thin and broadband layered microwave absorbing and shielding structures for commercial and defense applications. Funct Composit Struct 2019;1(3):032001.
[2] Pei H, Chen X, Huang X, Liu X, Zhang X, Huang Y. Key issues and algorithms of multiple-input-multiple-output over-the-air testing in the multi-probe anechoic chamber setup. Sci China Inf Sci 2022;65(3):1–27.
[3] AlShair R, AlSaket W, Faouri YS. Multi variant effects on the design of a microwave absorber and performance of an anechoic chamber. In: Proceedings of the 1st international congress on engineering technologies. CRC Press; 2021. p. 68–75.
[4] Sarin V, Vinesh P, Manoj M, Aanandan C, Mohanan P, Vasudevan K. Toroidal dipole-induced coherent forward scattering from a miniaturized cloaking structure. Appl Phys A 2020;126(2):1–8.
[5] Wang L, Ma Z, Zhang Y, Chen L, Cao D, Gu J. Polymer-based emi shielding composites with 3d conductive networks: a mini-review. SusMat 2021;1(3):413–31.
[6] Ling J, Zhai W, Feng W, Shen B, Zhang J, Zheng WG. Facile preparation of lightweight microcellular polyetherimide/graphene composite foams for electromagnetic interference shielding. ACS Appl Mater Interfaces 2013;5(7):2677–84.
[7] Yuan B, Bao C, Qian X, Song L, Tai Q, Liew KM, et al. Design of artificial nacre-like hybrid films as shielding to mitigate electromagnetic pollution. Carbon 2014;75:178–89.
[8] Chen J, Yi D, Jia X, Wang G, Sun Z, Zhang L, et al. Biomass-based aligned carbon networks with double-layer construction for tunable electromagnetic shielding with ultra-low reflectivity. J Mater Sci Technol 2022;103:98–104.
[9] Vovchenko L, Lozitsky O, Matzui L, Oliynyk V, Zagorodnii V. Microwave shielding and absorbing properties of single-and multilayered structures based on two-phase filler/epoxy composites. Appl Nanosci 2022;12(4):1037–49.
[10] Meisak D, Gurnevich E, Plyushch A, Bychanok D, Georgiev V, Kotsilkova R, et al. Robust design of compact microwave absorbers and waveguide matched loads based on dc-conductive 3d-printable filament. J Phys Appl Phys 2020;53(30):305301.
[11] Paddubskaya A, Bychanok D, Plyushch A, Kuzhir P, Nemilentsau A, Maksimenko S, et al. Epoxy resin/swcnt shielding paint for super-high-frequency range. J Nanoelectron Optoelectron 2012;7(1):81–6.
[12] Barani Z, Kargar F, Mohammadzadeh A, Naghibi S, Lo C, Rivera B, et al. Multifunctional graphene composites for electromagnetic shielding and thermal management at elevated temperatures. Adv Electro Mater 2020;6(11):2000520.
[13] Vovchenko L, Perets Y, Ovsienko I, Matzui L, Oliynyk V, Launetz V. Shielding coatings based on carbon–polymer composites. Surf Coating Technol 2012;211:196–9.
[14] Liu H-K, Yang R-B, Yen K-D. Radar-absorbing structures with reduced graphene oxide papers fabricated under various processing parameters. J Electron Mater 2022:1–10.
[15] Chen J, Wei Y, Zhao Y-T, Lin L, Li L, Su T. Transparent and broadband diffusion metasurface with high transparency and high shielding effectiveness using metallic mesh. IEEE Trans Antenn Propag 2022;70(7):5574–83.
[16] Chen P-Y, Farhat M, Ye Z, Amin M, Bagci H, Erricolo D. Artificial surfaces and media for electromagnetic absorption and interference shielding. 2021.
[17] Baah M, Paddubskaya A, Novitsky A, Valynets N, Kumar M, Itkonen T, et al. All-graphene perfect broadband thz absorber. Carbon 2021;185:709–16.
[18] Plyushch A, Macutkevic J, Svirskas S, Banys J, Plausinaitiene V, Bychanok D, et al. Silicon carbide/phosphate ceramics composite for electromagnetic shielding applications: whiskers vs particles. Appl Phys Lett 2019;114(18):183105.

[19] Jia Y, Chowdhury MAR, Zhang D, Xu C. Wide-band tunable microwave-absorbing ceramic composites made of polymer-derived sioc ceramic and in situ partially surface-oxidized ultra-high-temperature ceramics. ACS Appl Mater Interfaces 2019;11(49):45862–74.
[20] Jia Y, Chowdhury MAR, Xu C. Electromagnetic property of polymer derived sic–c solid solution formed at ultra-high temperature. Carbon 2020;162:74–85.
[21] Jia Y, Ajayi TD, Roberts MA, Chung C-C, Xu C. Ultrahigh-temperature ceramic–polymer-derived sioc ceramic composites for high-performance electromagnetic interference shielding. ACS Appl Mater Interfaces 2020;12(41):46254–66.
[22] Javid M, Qu X, Huang F, Li X, Farid A, Shah A, et al. In-situ synthesis of sic/fe nanowires coated with thin amorphous carbon layers for excellent electromagnetic wave absorption in ghz range. Carbon 2021;171:785–97.
[23] Li Y, Cao M-S, Wang D-W, Yuan J. High-efficiency and dynamic stable electromagnetic wave attenuation for la doped bismuth ferrite at elevated temperature and gigahertz frequency. RSC Adv 2015;5(94):77184–91.
[24] Li Y, Fang X, Cao M. Thermal frequency shift and tunable microwave absorption in bifeo3 family. Sci Rep 2016;6(1):24837.
[25] Bychanok D, Gorokhov G, Meisak D, Plyushch A, Kuzhir P, Sokal A, et al. Exploring carbon nanotubes/batio3/fe3o4 nanocomposites as microwave absorbers. Prog Electromagn Res C 2016;66(3):77–85.
[26] Wagh A. Chemically bonded phosphate ceramics: twenty-first century materials with diverse applications. Elsevier; 2016.
[27] Plyushch A, Kuzhir PP, Maksimenko SA, Macutkevič J, Banys J, Sokal A, et al. Grain size effect in conductive phosphate/carbon nanotube ceramics. Ceram Int 2017;43(6):4965–9.
[28] Mohan S, Joy P. Magnetic properties of sintered cofe2o4–batio3 particulate magnetoelectric composites. Ceram Int 2019;45(9):12307–11.
[29] Bouler J-M, Pilet P, Gauthier O, Verron E. Biphasic calcium phosphate ceramics for bone reconstruction: a review of biological response. Acta Biomater 2017;53:1–12.
[30] Trombetta R, Inzana JA, Schwarz EM, Kates SL, Awad HA. 3d printing of calcium phosphate ceramics for bone tissue engineering and drug delivery. Ann Biomed Eng 2017;45(1):23–44.
[31] Key B, Schroeder DJ, Ingram BJ, Vaughey JT. Solution-based synthesis and characterization of lithium-ion conducting phosphate ceramics for lithium metal batteries. Chem Mater 2012;24(2):287–93.
[32] Pavić L, Sklepić K, Skoko V, Tricot G, Mošner P, Koudelka L, et al. Ionic conductivity of lithium germanium phosphate glass-ceramics. J Phys Chem C 2019;123(38):23312–22.
[33] Wang W, Itoh S, Yamamoto N, Okawa A, Nagai A, Yamashita K. Electrical polarization of β-tricalcium phosphate ceramics. J Am Ceram Soc 2010;93(8):2175–7.
[34] Han R, Li J, Kong L, Liu J, Shan X, Cui X, et al. A novel phosphate-ceramic coating for high temperature oxidation resistance of ti65 alloys. Ceram Int 2019;45(18):23895–901.
[35] Ding Z, Li Y-Y, Xu M-R, Hong X, Hong S-X, Dong B. Electrochemical properties of aluminum tripolyphosphate modified chemically bonded phosphate ceramic anticorrosion coating. Construct Build Mater 2020;251:118874.
[36] Pleitt J, Colorado H, Castano C. Radiation shielding simulation for wollastonite-based chemically bonded phosphate ceramics. Adv Mater Sci Environ Energy Technol: Ceram Trans 2012;236:113–20.
[37] Colorado HA, Pleitt J, Yang J-M, Castano CH. Boron and lead based chemically bonded phosphates ceramics for nuclear waste and radiation shielding applications. Adv Mater Sci Environ Energy Technol II: Ceram Trans 2013;241:1–9.
[38] Vovchenko L, Lozitsky O, Oliynyk V, Zagorodnii V, Len T, Matzui L, et al. Dielectric and microwave shielding properties of three-phase composites graphite nanoplatelets/carbonyl iron/epoxy resin. Appl Nanosci 2020;10(12):4781–90.
[39] Vinnik D, Starikov AY, Zhivulin V, Astapovich K, Turchenko V, Zubar T, et al. Structure and magnetodielectric properties of titanium substituted barium hexaferrites. Ceram Int 2021;47(12):17293–306.
[40] Yakovenko OS, Matzui LY, Vovchenko LL, Oliynyk VV, Zagorodnii VV, Trukhanov SV, et al. Electromagnetic properties of carbon nanotube/bafe12- xgaxo19/epoxy composites with random and oriented filler distributions. Nanomaterials 2021;11(11):2873.
[41] Ismail MM, Rafeeq SN, Sulaiman J, Mandal A. Electromagnetic interference shielding and microwave absorption properties of cobalt ferrite cofe2o4/polyaniline composite. Appl Phys A 2018;124(5):1–12.
[42] Dabas S, Chahar M, Thakur O. Electromagnetic interference shielding properties of cofe2o4/polyaniline/poly (vinylidene fluoride) nanocomposites. Mater Chem Phys 2022;278:125579.
[43] Kumar A, Singh AK, Tomar M, Gupta V, Kumar P, Singh K. Electromagnetic interference shielding performance of lightweight nife2o4/rgo nanocomposite in x-band frequency range. Ceram Int 2020;46(10):15473–81.
[44] Tumarkin A, Tyurnina N, Tyurnina Z, Sinelshchikova O, Sviridov S, Gagarin A, et al. Composite structures basrtio3/nife2o4 for microwave applications. Ferroelectrics 2022;592(1):134–42.
[45] Vovchenko L, Lozitsky O, Matzui L, Oliynyk V, Zagorodnii V, Skoryk M. Electromagnetic shielding properties of epoxy composites with hybrid filler nanocarbon/batio3. Mater Chem Phys 2020;240:122234.
[46] Lozitsky O, Vovchenko L, Matzui L, Oliynyk V, Zagorodnii V. Microwave properties of epoxy composites with mixed filler carbon nanotubes/batio3. Appl Nanosci 2020;10(8):2759–67.
[47] Qing Y, Mu Y, Zhou Y, Luo F, Zhu D, Zhou W. Multiwalled carbon nanotubes–batio3/silica composites with high complex permittivity and improved electromagnetic interference shielding at elevated temperature. J Eur Ceram Soc 2014;34(10):2229–37.
[48] Qing Y, Ma L, Hu X, Luo F, Zhou W. Nife2o4 nanoparticles filled batio3 ceramics for high-performance electromagnetic interference shielding applications. Ceram Int 2018;44(7):8706–9.
[49] Plyushch A, Lewin D, Sokal A, Grigalaitis R, Shvartsman V, Macutkevič J, et al. Magnetoelectric coupling in nonsintered bulk batio3–xcofe2o4 multiferroic composites. J Alloys Compd 2022:165519.
[50] Nielsen E. Scattering by a cylindrical post of complex permittivity in a waveguide. IEEE Trans Microw Theor Tech 1969;17(3):148–53.
[51] Vaitkus A, Merkys A, Gražulis S. Validation of the crystallography open database using the crystallographic information framework. J Appl Crystallogr 2021;54(2):661–72. https://doi.org/10.1107/S1600576720016532.
[52] Şahin E. Microwave electromagnetic shielding effectiveness of znnb2o6-chopped strands composites for radar and wideband (6.5–18 ghz) applications. Lith J Phys 2022;62(3).
[53] Bhardwaj P, Grace AN. Antistatic and microwave shielding performance of polythiophene-graphene grafted 3-dimensional carbon fibre composite. Diam Relat Mater 2020;106:107871.

[54] Amutha Jeevakumari S, Mothilal T, Ramesh G, Arun Prakash V. Mechanically toughened emi shielding natural rubber composite in microwave frequency bands. Plast, Rubber Compos 2021;50(5):241–8.
[55] Ravel B, Stern E, Vedrinskii R, Kraizman V. Local structure and the phase transitions of batio3. Ferroelectrics 1998;206(1):407–30.
[56] Issa SA, Zakaly HM, Pyshkina M, Mostafa MY, Rashad M, Soliman T. Structure, optical, and radiation shielding properties of pva–batio3 nanocomposite films: an experimental investigation. Radiat Phys Chem 2021;180:109281.
[57] Havriliak S, Havriliak S. Comparison of the havriliak-negami and stretched exponential functions. Polymer 1996;37(18):4107–10.
[58] Fang P. Cole—cole diagram and the distribution of relaxation times. J Chem Phys 1965;42(10):3411–3.
[59] Svirskas S, Ivanov M, Bagdzevicius S, Macutkevic J, Brilingas A, Banys J, et al. Dielectric properties of 0.4 na0. 5bi0. 5tio3–(0.6-x) srtio3–xpbtio3 solid solutions. Acta Mater 2014;64:123–32.
[60] Svirskas Š, Adamchuk D, Grigalaitis R, Jablonskas D, Macutkevič J, Canu G, et al. Dipolar glass state in bace0. 3ti0. 7o3 perovskite solid solutions. J Alloys Compd 2021;854:155755.
[61] Plyushch A, Macutkevic J, Kuzhir P, Banys J, Bychanok D, Lambin P, et al. Electromagnetic properties of graphene nanoplatelets/epoxy composites. Compos Sci Technol 2016;128:75–83.
[62] Meisak D, Macutkevic J, Plyushch A, Kuzhir P, Selskis A, Banys J. Dielectric relaxation in the hybrid epoxy/mwcnt/mnfe2o4 composites. Polymers 2020;12(3):697.
[63] Plyushch A, Macutkevič J, Banys J, Kuzhir P, Kalanda N, Petrov A, et al. Carbon-coated nickel nanoparticles: effect on the magnetic and electric properties of composite materials. Coatings 2018;8(5):165.
[64] Belovickis J, Macutkevic J, Svirskas Š, Samulionis V, Banys J, Shenderova O, et al. Dielectric spectroscopy of polymer based pdms nanocomposites with zno nanoparticles. Ferroelectrics 2015;479(1):82–9.
[65] Pirc R, Blinc R. Vogel-fulcher freezing in relaxor ferroelectrics. Phys Rev B 2007;76(2):020101.
[66] Macutkevic J, Kuzhir PP, Paddubskaya AG, Banys J, Maksimenko SA, Stefanutti E, et al. Broadband dielectric/electric properties of epoxy thin films filled with multiwalled carbon nanotubes. J Nanophotonics 2013;7(1):073593.
[67] Svirskas Š, Banys J, Kojima S. Broadband dielectric spectroscopy of pb-based relaxor ferroelectric (1-x) pb (mg1/3nb2/3) o3-xpbtio3 with intermediate random fields. J Appl Phys 2017;121(13):134101.
[68] Belovickis J, Ivanov M, Svirskas Š, Samulionis V, Banys J, Solnyshkin AV, et al. Dielectric, ferroelectric, and piezoelectric investigation of polymer-based p (vdf-trfe) composites. Phys Status Solidi 2018;255(3):1700196.
[69] Chung B-K. Dielectric constant measurement for thin material at microwave frequencies. Prog Electromagn Res 2007;75:239–52.
[70] Chen L-F, Ong C, Neo C, Varadan V, Varadan VK. Microwave electronics: measurement and materials characterization. John Wiley & Sons; 2004.
[71] Kargar F, Barani Z, Balinskiy M, Magana AS, Lewis JS, Balandin AA. Dual-functional graphene composites for electromagnetic shielding and thermal management. Adv Electro Mater 2019;5(1):1800558.